Published in final edited form as:

Cell Rep. 2018 April 24; 23(4): 1005–1019. doi:10.1016/j.celrep.2018.03.098.

MIRO-1 Determines Mitochondrial Shape Transition upon GPCR Activation and Ca^{2+} Stress

Neeharika Nemani[1,2,12], **Edmund Carvalho**[1,2,12], **Dhanendra Tomar**[1,2,12], **Zhiwei Dong**[1,2], **Andrea Ketschek**[4], **Sarah L. Breves**[1,2], **Fabián Jaña**[1,2], **Alison M. Worth**[1,2], **Julie Heffler**[9], **Palaniappan Palaniappan**[1,2], **Aparna Tripathi**[1,2], **Ramasamy Subbiah**[1,2], **Massimo F. Riitano**[1,2], **Ajay Seelam**[1,2], **Thomas Manfred**[1,2], **Kie Itoh**[6], **Shuxia Meng**[5], **Hiromi Sesaki**[6], **William J. Craigen**[7], **Sudarsan Rajan**[1,2], **Santhanam Shanmughapriya**[1,2], **Jeffrey Caplan**[8], **Benjamin L. Prosser**[9], **Donald L. Gill**[10], **Peter B. Stathopulos**[11], **Gianluca Gallo**[4], **David C. Chan**[5], **Prashant Mishra**[3], and **Muniswamy Madesh**[1,2,13,*]

[1]Department of Medical Genetics and Molecular Biochemistry, Lewis Katz School of Medicine at Temple University, Philadelphia, PA 19140, USA

[2]Center for Translational Medicine, Lewis Katz School of Medicine at Temple University, Philadelphia, PA 19140, USA

[3]Children's Medical Center Research Institute, University of Texas Southwestern Medical Center, Dallas, TX 75390, USA

[4]Department of Anatomy and Cell Biology, Shriners Hospitals Pediatric Research Center, Lewis Katz School of Medicine at Temple University, Philadelphia, PA 19140, USA

[5]Division of Biology and Biological Engineering, California Institute of Technology, Pasadena, CA 91125, USA

[6]Department of Cell Biology, Johns Hopkins University School of Medicine, Baltimore, MD, USA

[7]Department of Molecular and Human Genetics, The Mitochondrial Diagnostic Laboratory, Baylor College of Medicine, Houston, TX 77030, USA

[*]Correspondence: madeshm@temple.edu.
[12]These authors contributed equally
[13]Lead Contact

AUTHOR CONTRIBUTIONS

N.N., E.C., Z.D., D.T., S.L.B., F.J., A.M.W., P.P., A.T., R.S., M.F.R., A.S., T.M., S.S., and M.M. performed and analyzed experiments involving biochemical, mitochondrial bioenergetics, and molecular and cellular experiments. N.N. and M.M. developed the MiST assay. N.N. and E.C. performed MiST imaging and analysis. Z.D. and D.T. performed immunoprecipitation and western blot analysis. A.K. and G.G. performed MiST imaging and analysis in primary neurons. J.H. and B.P. performed MiST imaging in primary cardiomyocytes. P.B.S. performed Miro EF structural analysis. J.C. performed EM imaging of ER-mitochondrial contact sites. S.M., P.M., and D.C.C. generated WT and MFF/Fis1 DKO MEFs. H.S. generated WT and Drp1 KO MEFs. W.J.C. generated WT and VDAC1/3 DKO MEFs. N.N., E.C., and S.R. cloned and generated plasmid constructs. N.N., E.C., and M.M. conceived, designed, analyzed, and interpreted experimental data. N.N., E.C., S.L.B., and M.M. wrote the manuscript with contributions from G.G., H.S., D.L.G., P.M., and D.C.C. All authors commented on the manuscript.

DECLARATION OF INTERESTS

The authors declare no competing interests.

SUPPLEMENTAL INFORMATION

Supplemental Information includes Supplemental Experimental Procedures, seven figures, and five videos and can be found with this article online at https://doi.org/10.1016/j.celrep.2018.03.098.

[8]Department of Biological Sciences, Delaware Biotechnology Institute, University of Delaware, Newark, DE 19711, USA

[9]Department of Physiology, University of Pennsylvania, Philadelphia, PA 19104, USA

[10]Department of Cellular and Molecular Physiology, Penn State Hershey College of Medicine, Hershey, PA 17033, USA

[11]Department of Physiology and Pharmacology, Western University, London, ON N6A 5C1, Canada

SUMMARY

Mitochondria shape cytosolic calcium ($[Ca^{2+}]_c$) transients and utilize the mitochondrial Ca^{2+} ($[Ca^{2+}]_m$) in exchange for bioenergetics output. Conversely, dys-regulated $[Ca^{2+}]_c$ causes $[Ca^{2+}]_m$ overload and induces permeability transition pore and cell death. Ablation of MCU-mediated Ca^{2+} uptake exhibited elevated $[Ca^{2+}]_c$ and failed to prevent stress-induced cell death. The mechanisms for these effects remain elusive. Here, we report that mitochondria undergo a cytosolic Ca^{2+}-induced shape change that is distinct from mitochondrial fission and swelling. $[Ca^{2+}]_c$ elevation, but not MCU-mediated Ca^{2+} uptake, appears to be essential for the process we term mitochondrial shape transition (MiST). MiST is mediated by the mitochondrial protein Miro1 through its EF-hand domain 1 in multiple cell types. Moreover, Ca^{2+}-dependent disruption of Miro1/KIF5B/tubulin complex is determined by Miro1 EF1 domain. Functionally, Miro1-dependent MiST is essential for autophagy/mitophagy that is attenuated in Miro1 EF1 mutants. Thus, Miro1 is a cytosolic Ca^{2+} sensor that decodes metazoan Ca^{2+} signals as MiST.

In Brief

Metazoan Ca^{2+} signal determines mitochondrial shape transition (MiST) and cellular quality control. Nemani et al. find that mitochondria undergo shape changes upon Ca^{2+} stress. MiST is distinct from matrix Ca^{2+}-induced swelling and mitochondrial dynamics. The conserved Ca^{2+} sensor Miro1 enables MiST and promotes autophagy/ mitophagy.

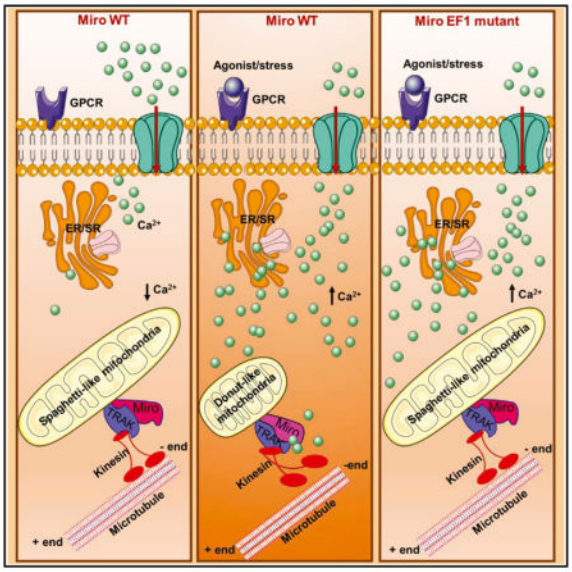

INTRODUCTION

Calcium is a ubiquitous second messenger that plays a pivotal role in virtually all unicellular and metazoan cells and is involved various physiologic processes including mitochondrial bioenergetics (Berridge et al., 2003; Soboloff et al., 2012). Although $_{c}Ca^{2+}$ shapes mitochondrial bioenergetics, elevated $_{c}Ca^{2+}$ drives $_{m}Ca^{2+}$ overload, which is a prerequisite for opening of the permeability transition pore (PTP), mitochondrial swelling, and necrotic cell death (Halestrap et al., 1993; Kroemer et al., 2007; Nicholls, 2005; Orrenius et al., 2003). Having established that mitochondria are multivariate signal processors in nearly all eukaryotes, the diverse functionality of mitochondria is reflected by their morphological complexity. This emphasized that understanding mitochondrial morphology changes in response to both physiological and pathological stress signals is essential. An observation made over seven decades ago revealed the plasticity of mitochondria, which appear as slender filaments under normal conditions (spaghetti-like) and break up into shorter segments (donut-like) when the cell is subjected to insult (Claude and Fullam, 1945). It has since been accepted that mitochondria are morphologically dynamic organelles that undergo constant fission and fusion (Bereiter-Hahn and Vöth, 1994; Yaffe, 1999). The phenotypic state of mitochondria has also been linked to their capacity for energy production, cell viability, and death mechanisms (Mishra and Chan, 2014; Youle and van der Bliek, 2012). While actively respiring mitochondria are long, tubular and filamentous, short circular fragmented mitochondria are often associated with pathological conditions, thus underscoring the importance of understanding mitochondrial shape changes (Mishra and Chan, 2014). Although mitochondrial fusion and fission events are fundamental for mitochondrial structure and dynamics, the process of mitochondrial shape transition (MiST) from spaghetti-like to donut-like is governed by unknown mechanisms during cellular activation.

Of the known proteins involved in mitochondrial dynamics such as MFN1, MFN2, Drp1, and OPA1 (Mishra and Chan, 2014), atypical small GTPase proteins have recently been proposed as key regulators of mitochondrial motility (Fransson et al., 2003, 2006; Reis et al., 2009). Miro1 and Miro2 are conserved single-pass transmembrane integral proteins with N-terminal regions exposed to the cytosolic side and consist of two GTPase domains separated by a pair of canonical EF hands (Birsa et al., 2013; Reis et al., 2009; Schwarz, 2013). Ca^{2+} binding to the cytosolic EF hands of Miro results in the halting of motile mitochondria on the microtubules upon stimulation (Macaskill et al., 2009; Nguyen et al., 2014; Saotome et al., 2008; Wang and Schwarz, 2009). Genetic deletion of the Miro1 resulted in postnatal lethality, underscoring the importance of the molecule and the existence of non-redundant roles of Miros (Nguyen et al., 2014). Loss of the yeast homolog of mammalian Miro1, Gem1p, causes aberrant mitochondrial distribution and morphology (Frederick et al., 2004). Interestingly, cytosolic Ca^{2+}-mediated mitochondrial length reduction has been proposed to be Drp1-independent mechanism (Tan et al., 2011). Although these findings support the view of mitochondria as dynamic in nature, the molecular mechanisms that mediate phenotypic changes during pathophysiological conditions remain unknown.

Here, we show that Miro1 senses $[Ca^{2+}]_c$ thereby triggering MiST with a K_d >1 μM $[Ca^{2+}]_c$. $[Ca^{2+}]_c$-induced MiST is selectively dependent on the Miro1 EF1 domain, but not Miro1 EF2 or Miro2, suggesting that EF1 provides the high-affinity Ca^{2+}-sensing mechanism that enables shape transitions independent of mitochondrial fission machinery. Miro1-dependent MiST is upstream and independent of MCU-mediated $[Ca^{2+}]_m$ uptake. The dynamic nature of the hetero-oligomeric MiST complex (Miro1/KIF5B/tubulin) is controlled by $[Ca^{2+}]_c$. These findings reveal a previously unknown mechanism of Miro1 as a component of MiST that is essential for quality control and autophagy.

RESULTS

$_cCa^{2+}$ Induces MiST Prior to PTP Opening and $\Delta\Psi_m$ Loss

To search for factor(s) residing on the mitochondrial surface that sense elevated $[Ca^{2+}]_c$ and elicit mitochondrial remodeling, we developed an image-based fluorescence assay for MiST using confocal microscopy. HeLa cells expressing mitochondrial matrix marker (COX8a-mRFP) were used to monitor MiST following $[Ca^{2+}]_c$ elevation. To separate the Ca^{2+}-induced MiST from the PTP opening and swelling, cells were loaded with the PTP opening indicator calcein-acetoxymethyl ester (calcein-AM) (Shanmughapriya et al., 2015). As depicted, both calcein and COX8a-mRFP signals overlaid in the mitochondria (Figure 1A). Upon ionomycin-induced $[Ca^{2+}]_c$ elevation, spaghetti-like mitochondria rapidly underwent donut-like morphological changes without any loss of calcein (Figure 1A). Following MiST, PTP opening occurred as evidenced by calcein fluorescence quenching due to $CoCl_2$ entry (Figures 1A and 1B; Video S1). Analysis of live-cell imaging data revealed that MiST precedes PTP opening in a temporal manner (Figure 1B) with a delay of ~120 s between MiST and PTP opening. To further establish that the assay we have developed resolves MiST from PTP opening, HeLa cells were pretreated with the PTP blocker cyclosporine A (5 μM) and exposed to ionomycin. Remarkably, ionomycin-induced $[Ca^{2+}]_c$ exhibited a similar MiST phenotype without any calcein fluorescence quenching, indicating that MiST

occurs prior to and independent of PTP opening (Figures 1C and 1D; Video S2). Although ionomycin-induced $_{m}Ca^{2+}$ loading did not elicit inner mitochondrial membrane (IMM) permeability (Figure 1E), the analysis of mitochondrial length showed that mitochondria >5 μm in length robustly transitioned to <2 μm in control and cyclosporine A (CSA)-treated conditions (Figures 1F and 1G). Together, these parameters affirm that this assay distinguishes MiST from PTP opening.

We next asked whether MiST occurs under physiological settings. To address this, HeLa and mouse embryonic fibroblasts (MEFs) were stimulated with G-protein coupled receptor (GPCR) agonists, histamine and thrombin that trigger $_{c}Ca^{2+}$ dynamics (Figure 1H, left). Analysis of mitochondrial length revealed a reversible MiST that correlates with $[Ca^{2+}]_c$ dynamics. In contrast, a sustained increase in $[Ca^{2+}]_c$ by ionomycin resulted in irreversible MiST (Figure 1H, right). To examine whether $[Ca^{2+}]_c$-induced MiST was prior to $\Delta\Psi_m$ loss, COX8a-mRFP-expressing HeLa and MEFs were loaded with $\Delta\Psi_m$ indicator DHR123, and changes were monitored. Analysis of $\Delta\Psi_m$ and mitochondrial length revealed MiST occurrence at ~120–150 s but with intact $\Delta\Psi_m$, suggesting that MiST was not a consequence of $\Delta\Psi_m$ loss (Figures 1I and S1A–S1C). To test whether dissipation of $\Delta\Psi_m$ promotes MiST, HeLa and MEFs treated with carbonilcyanide *p*-trifluoromethoxyphenylhydrazone (FCCP) caused a rapid loss of $\Delta\Psi_m$ without any effect on mitochondrial morphology (Figures S1D and S1F). These data indicate that MiST is $[Ca^{2+}]_c$ dependent and upstream of PTP opening.

$_{c}Ca^{2+}$-Induced MiST Is Upstream and Independent of MCU-Dependent Mitochondrial Ca^{2+} Uptake

Due to the unique biophysical nature of mitochondrial Ca^{2+} uniporter (MCU), MCU complex-dependent mitochondrial Ca^{2+} uptake is the major mechanism for the rapid clearance of $[Ca^{2+}]_c$ (Baughman et al., 2011; De Stefani et al., 2011). Conversely, MCU-mediated $[Ca^{2+}]_m$ overload promotes PTP opening, leading to organelle swelling (Orrenius et al., 2003). Recent studies established that genetic deletion of MCU-abrogated $[Ca^{2+}]_m$ uptake and resulted in sustained $[Ca^{2+}]_c$ elevation (Mallilankaraman et al., 2012; Pan et al., 2013). Given its crucial role in $[Ca^{2+}]_c$ clearance and $[Ca^{2+}]_m$ uptake, we investigated a link between MiST and MCU. As expected, MCU KD cells exhibited reduced $[Ca^{2+}]_m$ uptake (Figure S1M) but were unable to clear $[Ca^{2+}]_c$ (Figure 2C). Our data indicate that MiST occurrence is temporally faster in MCU KD cells compared to control (Figures 2A and 2B). To further examine whether increased $[Ca^{2+}]_m$ retention capacity drives MiST, we utilized the cyclophilin D knockout ($CypD^{-/-}$) MEFs, where PTP remains closed but retains higher levels of $[Ca^{2+}]_m$. Similar to MCU deletion, loss of CypD did not prevent $[Ca^{2+}]_c$-induced MiST (Figures 2A–2C). These results indicate that MiST is not due to $_{m}Ca^{2+}$ but rather $[Ca^{2+}]_c$-dependent.

To further exclude the role of MCU in MiST, we utilized MCU knockout (KO) hepatocytes (Figure 2D). Hepatocytes were labeled with DHR123 that served as a MiST indicator (Figure 2F). When DHR123-stained $MCU^{fl/fl}$ and MCU KO hepatocytes were MCU KO hepatocytes, suggesting that $[Ca^{2+}]_m$ triggers PTP opening but not MiST (Figure 2G). Having observed robust MiST in MCU KO, we further investigated mitochondrial

remodeling *in situ* by ultra-structural imaging. EM images acquired from liver tissues from control and MCU KO mice showed a significant increase in the MiST-like phenotype when compared to control (Figures 2H and 2I). To further establish that $[Ca^{2+}]_c$ agonist induces MiST, extra- or intracellular Ca^{2+} was chelated using EGTA and BAPTA-AM (Figures S1G and S1J). As expected, ionomycin-induced intracellular $[Ca^{2+}]_c$ rise was ablated in BAPTA-treated cells (Figure S1H). Chelation of extracellular Ca^{2+} by EGTA resulted in transient $[Ca^{2+}]_c$ rise when compared to control (Figure S1K). Intriguingly, MiST was inhibited in cells treated with either BAPTA-AM (25 μM) or EGTA (0.5 mM) (Figures S1I and S1L). These data again reinforce that $[Ca^{2+}]_c$ elicits MiST and was without any effect by $[Ca^{2+}]_m$.

To gain further insights into the role of $[Ca^{2+}]_c$ in MiST, we asked whether the loss of MCU could result in MiST following GPCR agonist stimulation. We analyzed MiST after stimulation with histamine (100 μM) and found the rate of MiST to be greater in MCU KD but not wild-type further strengthening the idea that $[Ca^{2+}]_c$ is an initiator of MiST (Figures S1N–S1P). Measurement of intracellular Ca^{2+} ($[Ca^{2+}]_i$) in cells stimulated with histamine and thrombin caused transient (~3–6 μM) $[Ca^{2+}]_i$ while ionomycin resulted in sustained (~6 μM) $[Ca^{2+}]_i$ rise (Figures S1Q and S1R). The kinetics of $[Ca^{2+}]_i$ rise is consistent with the rate of MiST (Figures S1O and 1H). To further distinguish MiST from mitochondrial swelling, MEFs knocked out for other components of mPTP (VDAC$^{1/3}$ DKO and SPG7 KO), and apoptotic gatekeepers Bax and Bak (Bax/Bak DKO) were transfected with mitochondrial marker and challenged with ionomycin (Figure S2). Preventing PTP opening (SPG7 KO, VDAC$^{1/3}$ DKO) or outer mitochondrial membrane (OMM) permeabilization did not have any effect on MiST with comparable MCU-mediated $[Ca^{2+}]_m$ uptake (Figures S2A–S2C), Together, these results indicate that $[Ca^{2+}]_c$ is a prerequisite for MiST and is an upstream event of $[Ca^{2+}]_m$-mediated PTP opening.

$_cCa^{2+}$-Induced MiST Is Less Likely Dependent on Cytoskeletal Remodeling and Reactive Oxygen Species

Mitochondrial distribution in cells is mediated by interaction with the cytoskeleton. Hence, we asked whether cytoskeletal disruption could also result in MiST. HeLa cells were co-transfected with tubulin-GFP and COX8A-mRFP to observe the spaghetti-like mitochondrial distribution along the tubulin-GFP track (Figure 3A; Video S3). Following ionomycin stimulation, we observed $[Ca^{2+}]_c$-induced MiST without any effect on tubulin-GFP remodeling (Figures 3A, 3C, and 3D). We next tested whether microtubule de-polymerization by colchicine could replicate the MiST-like phenotypic changes (Figure 3B). To confirm the colchicine effect, HeLa cells with 1 μM colchicine caused a disruption of microtubule network (Figure S3C). Treatment with colchicine caused perinuclear aggregate-like phenotype rather than MiST (Figures 3B, as indicated in inset, 3C, and 3D). Spatial distribution of mitochondria in the cell is dependent on kinesin family of motor proteins (Tanaka et al., 1998). To address whether loss of KIF5B phenocopies MiST, we silenced KIF5B using small interfering RNA (siRNA) (Figure 3G). Consistent with previous findings (Tanaka et al., 1998), we observed that loss of KIF5B resulted in perinuclear aggregation of mitochondria (Figure 3E). Upon stimulation, the aggregated mitochondria still underwent MiST (Figures 3E, 3F, S3A, and S3B).

Next, to examine whether disrupting actin filaments and myosin trigger MiST, we employed latrunculin A (Lat A) and blebbistatin that cause actin and myosin II depolymerization (Boldogh and Pon, 2006). Similar to colchicine treatment, Lat A caused mitochondrial aggregation without change in mitochondrial shape (Figures S3D, S3E, bottom, and S3G). Accordingly, treatment with blebbistatin alone did not trigger MiST (Figures S3E, top, and S3G). The occurrence of $[Ca^{2+}]_c$-induced MiST was still observed in blebbistatin-pretreated HeLa cells (Figures S3F and S3G). Together, these results indicate that $[Ca^{2+}]_c$-induced MiST is not determined by cytoskeletal disruption.

To examine whether Ca^{2+}-induced reactive oxygen species (ROS) contributes to MiST, HeLa cells were pretreated with glutathione ester (5 mM) or N-Acetyl cysteine (NAC; 10 mM) before stimulation (Figures 3H and 3I). Surprisingly, antioxidant-treated cells exhibited MiST (Figures 3J and 3K). Additionally, HeLa cells transfected with a combination of AdMnSOD and peroxiredoxin (Prdx3) to quench mitochondrial reactive oxygen species (mROS) also underwent MiST (Figure 3L) indicating that ROS is not required for $[Ca^{2+}]_c$-induced MiST. Furthermore, mitochondrion level analysis strongly indicates MiST phenotype to be distinct from fragmentation (Figure 3M).

Cytosolic Ca^{2+}-Induced MiST Is Independent of Drp1-Dependent Mitochondrial Fission

Mitochondrial shape and interconnectivity is mediated by both fission and fusion mechanisms. Drp1 is a member of the dynamin family of GTPases that participates in mitochondrial fragmentation by phosphorylation at two different conserved sites, serine 600 and serine 579 in isoform 3 (S637 and S616 of Drp1 isoform1) (Cereghetti et al., 2008; Cribbs and Strack, 2007). We utilized pharmacological and genetic tools to examine whether the $[Ca^{2+}]_c$-induced dephosphorylation of Drp1 is pertinent to MiST. HeLa cells pretreated with the calcineurin inhibitor FK506 did not show a difference in the kinetics or magnitude of MiST upon stimulation with similar $[Ca^{2+}]_c$ dynamics (Figures S4A–S4C). Stable cells expressing Drp1 mutants (S600A, S600D, S579A, and S579D) displayed similar $[Ca^{2+}]_c$ and $[Ca^{2+}]_m$ and also underwent MiST upon stimulation, further re-enforcing that MiST is independent of Drp1-mediated mitochondrial fission (Figures S4D–S4I). Having observed limited effect for phosphatase-dependent Drp1 activation on $[Ca^{2+}]_c$-induced MiST, we next sought to understand the importance of MiST in Drp1 KO MEFs. As expected, Drp1 KO MEFs displayed a highly elongated mitochondrial phenotype (Figure 4A). Cells expressing COX8a mRFP were stimulated and MiST was monitored (Figure 4C). Remarkably, Drp1 KO mitochondria underwent MiST following $[Ca^{2+}]_c$ mobilization without any change in Ca^{2+} dynamics, indicating that Drp1 is not required in $[Ca^{2+}]_c$-induced MiST (Figures 4B and 4D–4F). To further confirm that Ca^{2+}-induced MiST is distinct from mitochondrial fragmentation, we used MFF/Fis1 DKO MEFs (Losón et al., 2013). Similar to Drp1 KO MEFs, ionomycin stimulation caused both the wild-type (WT) and DKO cells to undergo MiST (Figures 4G, 4J, and 4K) with similar $[Ca^{2+}]_c$ mobilization and $[Ca^{2+}]_m$ uptake (Figures 4G–4I).

To address whether components of the dynamin family play a role in MiST, we performed MiST analysis in RNAi knockdown of Dyn2 and adaptor proteins Mid51 and Mid49 in MEFs (Lee et al., 2016; Palmer et al., 2011) (Figures S4J and 4L). Upon stimulation, Dyn2,

Mid 49, and Mid 51 siRNA-treated MEFs underwent MiST with a similar rise in $[Ca^{2+}]_c$ and $[Ca^{2+}]_m$ (Figures 4M–4R). Collectively, these results indicate that mitochondria undergo shape change from spaghetti-like to donut-like when subjected to high $[Ca^{2+}]_c$, which are independent of the fission machinery (Figure 4S).

Outer Mitochondrial Membrane Anchored Miro1 EF-1 Hand Domain Exclusively Senses $[Ca^{2+}]_c$ and Promotes MiST

To identify the OMM Ca^{2+}-sensing factor that is likely embedded on the OMM to promote MiST upon $_cCa^{2+}$ elevation, we searched in MitoCarta and MitoMiner mitochondrial proteome libraries (Pagliarini et al., 2008; Smith et al., 2012). Miro GTPases were identified as atypical Rho GTPases residing in the OMM at their C-terminal region and comprising a pair of Ca^{2+}-sensing EF-hand domains. It has been shown that Miro, Milton (TRAK1), and Kinesin form the transport complex at the cytosolic and mitochondrial junction for mitochondrial movement in neurons (Macaskill et al., 2009; Saotome et al., 2008; Wang and Schwarz, 2009). Since Miro proteins contain EF-hand domains, we speculated that high-affinity Ca^{2+} binding by the EF hands enables Miro to sense elevated $_cCa^{2+}$ (Figures 5A and 5H). To examine whether disruption of the EF-hand domains prevents MiST in response to $_cCa^{2+}$, we first generated MEFs stably expressing four different Miro1 EF1 and EF2, Miro2 EF1 and EF2 hand mutants by introduction of two point mutations of crucial acidic amino acids that disable Ca^{2+} binding (Flag-tagged M1WT, M1EF1, M1EF2, M2WT, M2EF1, and M2EF2 mutants) (Figures 5A, 5B, 5H, and 5I). These MEFs were challenged with ionomycin, and MiST was monitored (Figures 5C and S5A). MEFs expressing either M1WT or M1EF2 mutant MEFs yielded a similar kinetics of MiST (Figures 5C and 5F; Video S4). Remarkably, MEFs expressing M1EF1 mutant did not undergo MiST (Figures 5C and 5F; Video S5), but the $[Ca^{2+}]_c$ and $[Ca^{2+}]_m$ dynamics were comparable in all conditions (Figures 5D and 5E). Surprisingly, disabling EF-hand domains of Miro 2 did not prevent the ionomycin-induced MiST, although M2EF2 mutant delayed but eventually triggered MiST (Figures S5A and 5L). Similar to Miro1, Miro2 mutants showed normal $[Ca^{2+}]_c$ release and $[Ca^{2+}]_m$ uptake (Figures 5J and 5K). Although M1EF1 cells failed to promote MiST, GPCR-mediated $[Ca^{2+}]_c$ and $[Ca^{2+}]_m$ dynamics remained unaltered (Figures S5E–S5H). Although the Miro1 EF1 mutant prevented MiST, the protein-protein interaction between the WT Miro1 and Miro1 EF1 mutant remained unaffected (Figure 5N). Together, these data indicate the non-redundant contribution of Miro1 EF1 in Ca^{2+}-sensing and MiST phenotype (Figures 5G and 5M). To further confirm the overexpression results, we adapted a genome-editing (CRISPR/Cas9; nickase) strategy to generate a loss-of-function of Miro1 EF1 (Figures 5O and 5P). Functional analysis of M1EF1 displayed similar phenotype to that of M1EF1-overexpressing cells (Figure 5R); however, Ca^{2+} dynamics and $\Delta\Psi_m$ are unaltered in Miro1 EF1 KI MEFs (Figures 5Q, 5S, and 5T). These results further strengthen our findings that Miro1 EF1 is the determinant of $[Ca^{2+}]_c$-induced MiST.

Sequence alignment of the 12-residue Ca^{2+}-coordinating loops of Miro1 and Miro2 canonical EF hand 1 shows nonconserved residues at loop positions 4, 6, 7, 9, and 11 (Figure S5B). Among these positions, only position 9 is directly involved in canonical Ca^{2+} coordination via a main chain, non-bonded interaction with Ca^{2+}. However, position 6 encodes a highly invariant Gly residue, which is conserved in Miro1 EF1, but not in Miro2

EF1 or Miro1 EF2 (Figure S5B). This invariant Gly permits the peptide backbone to undergo an abrupt turn, which promotes ideal Ca^{2+} coordination geometry. Variation of this Gly reduces the Ca^{2+} binding affinity of canonical EF hands (Allen et al., 2014). Homology model reveals that the Asn205 (human numbering) is involved in stabilizing the vital Glu208 position in Ca^{2+} coordination for Miro1, whereas Miro2 does not exhibit this stabilizing interaction due the presence of a shorter Ser side chain at this position (Figure S5C). A similar analysis of human Miro1 and Miro2 EF2 only shows sequence divergence at positions 2, 6, and 11 (Figure S5B) and the H-bonding network at the three-dimensional structural level remains conserved, despite these sequence differences (Figure S5D). Together, these data reveal the non-redundant role of Miro proteins in the context of MiST.

Since Miro1 constitutes conserved functional GTPase domains (Fransson et al., 2003), we next assessed whether the GTPase domain participates in $[Ca^{2+}]_c$-dependent MiST. Interestingly, of the two GTPase domains, it has been shown that GTPase 1 plays a predominant role and hence we used two mutated forms of this domain (Fransson et al., 2003). HeLa cells stably expressing Flag-tagged M1T18N and M1P13V underwent MiST without any change in Ca^{2+} dynamics (Figures S5I–S5N) suggesting that Miro1 GTPase activity is dispensable for Ca^{2+}-induced MiST. We also tested whether higher dose of ionomycin-induced $[Ca^{2+}]_c$ activates other EF hands of Miro1 or Miro2. Interestingly, stable M1EF1 mutant expressing MEFs did not undergo MiST indicating the crucial role for Miro1 EF1 in Ca^{2+}-sensing and eliciting MiST (Figures S5O–S5Q). Since Miro 1 EF1 mutant prevented MiST, we investigated to see whether mutations in Miro would still undergo mitochondrial fragmentation. MEFs stably expressing Flag-tagged M1WT and M1EF1 mutant were subjected to oligomycin (10 μM) + Antimycin A (10 μM) for 4 hr and exhibited mitochondrial fragmentation (Figure S5R). These data demonstrate that Miro1 EF1 is not deficient in mitochondrial fragmentation but prevents mitochondria from high $[Ca^{2+}]_c$-induced MiST.

Further, we tested MiST in primary cell types including sensory and hippocampal neurons. Cultured sensory neurons loaded with MitoTracker Green underwent MiST upon stimulation (Figure S5S). Similar to MEFs, neurons expressing M1EF1 did not undergo MiST, while WT Miro1-expressing neurons exhibited MiST (Figures S5T and S5U). Glutamate toxicity triggers mitochondrial-dependent neuronal death through elevation of $[Ca^{2+}]_{c,}$ (Brustovetsky et al., 2009; Rintoul et al., 2003). As expected, neurons exhibited $[Ca^{2+}]_i$ elevation following glutamate addition (Figure S5V). Hippocampal neurons expressing Miro1 EF1 mutant exhibited a significant reduction of MiST when challenged with glutamate (Figure S5W). These results indicate that Miro1 is required for the progression of MiST in multiple cell types including neurons. Having observed MiST in neuronal cells, we have further validated MiST in primary adult cardiomyocytes (Figures S5X and S5Y). This provides strong support that MiST is a conserved mechanism that is observed in multiple cell types.

Disruption of Miro1/Kinesin/Tubulin Complex but Not Endoplasmic Reticulum/Mito Contact Sites in MiST

Because Miro1 EF1-hand controls $[Ca^{2+}]_c$-induced MiST, we next examined whether oligomeric nature of Miro1 is altered upon Ca^{2+} binding. Cell lysates from MEFs expressing

Miro1 WT or M1EF1 treated with or without ionomycin were subjected to fast protein liquid chromatography (FPLC) profiling. Although Miro1 WT and Miro1 EF1 mutant interact, the FPLC analysis revealed that the oligomeric nature of Miro1 and its mutant were not disrupted upon $[Ca^{2+}]_c$ elevation (Figure 6A) suggesting that the loss of Ca^{2+} binding did not alter the Miro1 oligomeric complex. Building on the existing models of mitochondrial motility (Wang and Schwarz, 2009; Macaskill et al., 2009), we next studied the molecular nature of MiST. WT MEFs were co-transfected with hemagglutinin (HA)-tagged M1WT/M1EF1/ M1EF2/M2WT/M2EF1/M2EF2 and Flag tagged-KIF5B (Figure 6B). Immunoprecipitation of Miro and its mutants with an antibody specific for Flag followed by western blotting revealed that Miro1/2 and its EF mutants interact with kinesin both in the presence and absence of Ca^{2+} (Figure 6B). Either interaction of KIF5B/tubulin or Miro/tubulin was disrupted in the presence of Ca^{2+} but that was intact exclusively in M1EF1 (Figure 6B) suggesting that MiST results in release of mitochondria from tubulin but not motor protein. Since Miro proteins form a hetero-oligomeric complex, we next tested whether Miro proteins bind to mitochondrial dynamics components. Co-immunoprecipitation assay reveals that only Miro2 but not Miro1 interacts with Mfn1 and Mfn2 (Figure 6C). We also determined whether Drp1 interacts with Miro1 and 2 and found no interaction with Drp1 (undetectable). It is plausible that Miro1 is exclusively involved in MiST.

We next asked whether Ca^{2+}-induced MiST is associated with endoplasmic reticulum (ER)-mitochondrial contact site disruption. Ionomycin stimulation of M1WT and M1EF1 Cos7 cells expressing Mito-Red and GFP-Sec61β did not have any effect on ER network and ER-mito contact sites (Murley et al., 2013; Rowland and Voeltz, 2012) (Figures S6A–S6D). These data were substantiated by electron microscopic data that revealed no change in ER-mito contact sites (Figure S6E). Finally, M1WT and M1EF1 mutant cells exhibited XBP1s and ATF6a processing after thapsigargin and ionomycin treatment suggesting the normal ER function (Figures S6F and S6G).

Miro1-Dependent Ca^{2+}-Induced MiST Is Essential for Mitochondrial Quality Control

Having shown the abrogation of $[Ca^{2+}]_m$ uptake is dispensable for MiST (Figure 2), we next asked whether mitochondrial shape change had any effect on autophagy. MEFs expressing M1WT and M1EF1 mutant were co-transfected with cox8a-mRFP and GFP-LC3 and stimulated with thrombin or ionomycin (Figures 7A and 7C). Upon $[Ca^{2+}]$ mobilization, M1WT but not M1EF1 displayed MiST followed by the translocation of GFP-LC3 in M1WT cells, suggesting that a shape change occurs prior to LC3 tethering to the mitochondria (Figures 7A–7D). Kinetic analysis of GFP-LC3 translocation revealed that $[Ca^{2+}]_c$ is the determinant of MiST-mediated autophagosome formation (Figure 7E). Consistent with imaging data, M1EF1 mutant MEFs did not process LC3 and p62 when subjected to starvation (24 hr) or ionomycin stimulation (4 hr) (Figures S7D–S7F).

Delivery of the autophagic substrate to the lysosome and the degradation of the substrate in the lysosome is an essential step for autophagic flux. MEFs were transduced with AdGFP-RFP-LC3. Starvation and Ca^{2+}-induced autophagy resulted in increased autophagic flux as seen in increased GFP^+ puncta and RFP^+/GFP^+ puncta in control and EF mutants but not in

M1EF1 (Figures S7G and S7H), suggesting that MiST is required for autophagic flux. Ionomycin stimulation of 3MA (autophagy inhibitor)-pretreated HeLa cells still underwent MiST (Figures S7K and S7L) indicating that MiST is a requisite for downstream autophagy. To provide a mechanistic link between MiST and autophagosome formation, we asked whether MiST facilitates lipid transfer from mitochondria (Hailey et al., 2010). It was observed that under starvation M1WT and M1EF1 mutant MEFs expressing Mito-BFP and mCherry-LC3 and then loaded with NBD-PS displayed mCherry-LC3/NBD-PS/Mito-BFP overlay in M1WT but not in M1EF1 (Figures 7F–7H) suggesting that MiST is required for supplying lipids for autophagosome formation.

Because MiST is essential for mitochondrial quality control, we next monitored Parkin-mediated mitophagy in a Ca^{2+}-dependent process (Narendra et al., 2008). MEFs expressing Parkin-mCherry and Mito-EGFP were stimulated with ionomycin. M1WT but not M1EF1 mutant MEFs exhibited MiST (Figures 7I and 7J) with no localization of Parkin to the mitochondria (Figures 7I and 7J). Unlike ionomycin treatment, FCCP resulted in localization of Parkin-mCherry to the mitochondria in both M1WT and M1EF1 mutant MEFs (Figures 7K–7M and S7I). Although $\Delta\Psi_m$ dissipation by FCCP results in matrix $[Ca^{2+}]_m$ release (~0.6 μM), it is below the threshold to elicit MiST (Figure S7J). To further understand whether MiST was required for autophagic clearance of mitochondria, MEFs were subjected to ionomycin, FCCP, and starvation. Western blot analysis revealed a decrease in mitochondrial Tom20, cytochrome *c*, and MCU proteins in M1WT but not in M1EF1 mutant with ionomycin stimulation suggesting that MiST facilitates autophagic clearance (Figure 7N). Furthermore, MEFs expressing Mito-EGFP and LAMP1-mCherry (lysosomes) were subjected to ionomycin for 4 hr and imaged for mitophagy as evidenced by lysosomal localized mitochondria (Figures 7O–7R). Consistent with autophagic clearance data (Figure 7N), M1WT but not M1EF1 displayed lyso/mito phagosome formation indicating the importance of MiST in organelle quality control. Although Parkin-induced mitophagy is $\Delta\Psi_m$ dependent, our data reveal that Ca^{2+}-induced MiST is independent of $\Delta\Psi_m$ and augments mitophagy.

To examine whether maintaining spaghetti-like mitochondria under conditions of elevated $[Ca^{2+}]_c$ has any effect on cellular bioenergetics and cell viability, MEFs were subjected to oxygen consumption rate (OCR). The OCR measurement revealed that EF-hand mutation did not alter the bioenergetic parameter suggesting the mitochondrial function is maintained under resting conditions (Figures S7A–S7C). It is important to note that the reconstitution of Miro1 WT exhibited modestly higher OCR under maximal stimulation of electron transport chain activity by uncoupler (Figure S7C). Additionally, MEFs stimulated with thrombin revealed an increase in OCR, ATP, and mROS production, but no significant difference in the bioenergetics parameters between the groups was observed (Figures S7M–S7Q). Consequently, the rate of NADH production also remained the same in M1WT and M1EF1 mutant MEFs (Figure S7R). Together, these results suggest that mutating the EF hand of Miro1 does not alter cellular bioenergetics. Since MCU-mediated $[Ca^{2+}]_m$ overload is also known to induce cell death through PTP opening (Halestrap et al., 1993), first, we investigated whether preventing either OMM or IMM permeabilization would offer protection from Ca^{2+}-induced cell death. Surprisingly, $[Ca^{2+}]_c$-induced cell death was not prevented in primary MCU KO endothelial cells suggesting that preventing $[Ca^{2+}]_m$

overload is not sufficient to preserve cell viability (Figure S7S). Similarly, deletion of Bax/Bak in MEFs did not prevent ionomycin-induced cell death (Figure S7T). To understand whether loss of $[Ca^{2+}]_c$ sensing of Miro1 could prevent MiST-dependent cell death, MEFs were challenged with ionomycin and cell viability assessed by flow cytometry. Strikingly, the ionomycin-induced cell death was significantly reduced in MEFs expressing M1EF1 mutant when compared to other counter parts (Figure S7U). We next asked whether the loss of $[Ca^{2+}]_c$ sensing by Miro1 and $[Ca^{2+}]_m$ uptake exhibits synergistic effect on cell viability. MCU KD HeLa cells expressing M1EF1 were challenged with ionomycin. We observed that blocking $[Ca^{2+}]_m$ overload did not offer any additive effect on cell viability (Figure S7V).

DISCUSSION

Cytosolic Ca^{2+} dynamics not only govern cellular functions including cell survival and death, but also control organelle structure and function (Berridge et al., 2003; Clapham, 2007). To evade the elevated $[Ca^{2+}]_c$-dependent signals, mitochondria rapidly clear $[Ca^{2+}]_c$ through the MCU channel during activation (De Stefani et al., 2011). Remarkably, ablation of MCU-mediated $[Ca^{2+}]_m$ uptake failed to prevent the $[Ca^{2+}]_c$-induced cell death (Pan et al., 2013) and (Figure S7). Our findings identify a mechanism that occurs either prior to or as a result of abrogation of $[Ca^{2+}]_c$ clearance that we termed MiST. The presumption has been that changes in mitochondrial morphology due to PTP opening and swelling as a result of $[Ca^{2+}]_m$ overload (Kroemer et al., 2007; Orrenius et al., 2003; Shanmughapriya et al., 2015). Here, we now reveal that the mitochondrial resident cytosolic Ca^{2+} sensor Miro1 defines exquisite specificity for MiST that occurs in response to changes in $[Ca^{2+}]_c$.

To differentiate MiST from mitochondrial swelling, we developed an assay where mitochondrial swelling was observed as a release in calcein fluorescence and MiST was monitored as the change in the length of the mitochondria. Upon robust $[Ca^{2+}]_c$ elevation, MiST followed by PTP opening was observed spatiotemporally, suggesting that MiST is upstream of mitochondrial swelling. Although the prediction was that inhibiting PTP pathways would halt mitochondrial remodeling, our data illustrate that either preventing PTP opening by genetic and pharmacologic approaches or blocking $[Ca^{2+}]_m$-uptake did not prevent $[Ca^{2+}]_c$-induced MiST (Figures 1, 2 and S2) (Baines et al., 2005; Pan et al., 2013), further strengthening our argument of MiST that is $[Ca^{2+}]_c$ elevation but not $[Ca^{2+}]_m$ uptake. The lack of protection from cell death observed in MCU KO animals (Pan et al., 2013) could possibly be due to elevated $[Ca^{2+}]_c$ that binds the EF-hand domain of Miro1 and elicits MiST (Figure 5). Since MCU KO cells did not show protection to necrotic death and only a modest reduction in the susceptibility was observed in M1EF1 mutant cells to ionomycin-induced cell death, we speculate that preventing MiST and PTP opening simultaneously may have synergistic effects. In support of this notion, cell death assay in MCU KD stably expressed with M1EF1 mutant, but not M1WT, demonstrated a significant protection against ionomycin-induced cell death suggesting the multiple factors involved mitochondrial phenotypic change (Figure S7). Interestingly, results from our investigations revealed that MiST occurs in response to sustained elevation of $[Ca^{2+}]_c$, and this phenomenon can be reversed by Ca^{2+} sequestrants (Figure S1). Mitochondrial morphology has been reported to be due to the transition between fission and fusion events (Bereiter-Hahn and Vöth, 1994;

Detmer and Chan, 2007). Either ablating Drp1 or the receptor for Drp1, MFF, and Fis1 or the other fission adaptor proteins promote mitochondrial elongation and reprograms mitochondrial metabolism and cell viability (Cereghetti et al., 2008; Cribbs and Strack, 2007; Losón et al., 2013; Palmer et al., 2011). Importantly, $[Ca^{2+}]_c$-induced MiST does not appear to utilize these strategies (Figures 4 and S4).

The GTPase domain of Miro1 is required to recruit Milton/ TRACK1, which binds kinesin heavy chain (KHC) to form the transport machinery (Schwarz, 2013). Though several lines of evidence suggest Miro1 might be involved in mitochondrial motility, the role of Miro GTPases in modulating mitochondrial shape has been largely unknown. Yeast Miro1 homolog Gem1p was described to be associated with mitochondrial morphology. Gem1pΔ cells exhibited aberrant mitochondrial morphology ranging from circular grape-like to tubular (Frederick et al., 2004). Our results suggest that mutating specifically EF1 domain of Miro1 but not EF2/Miro2/GTPase desensitizes mitochondria from sensing the elevated $[Ca^{2+}]_c$ and hence prevents $[Ca^{2+}]_c$-induced MiST. It is important to highlight that the higher levels of $[Ca^{2+}]_c$ also does not elicit MiST in M1EF1 mutant cells suggesting that this site could be the major Ca^{2+} sensor that promotes MiST (Figures 5, 6, and S5).

Ca^{2+} and redox signaling are intimately linked to mitochondrial bioenergetics (Denton, 2009; Halestrap et al., 1993). Aberrations of proximal signals elicit cell death via necrosis, apoptosis, and autophagy. Our spatiotemporal resolution of the two processes defineMiSTasaprecursorof$[Ca^{2+}]_i$-inducedautophagy(Figure7). This event is supported by M1EF1 MEFs, where autophagosomes formation is defective due to the lack of MiST. Moreover, our data reveal that MiST is essential to supply lipids for autophagosome formation. Enigmatically, ultra-structure images of MCF7 cells treated with purinergic receptor agonist, ATP or ionomycin, elicited varying levels of autophagosome formation, that corroborates with our findings (Høyer-Hansen et al., 2007) (Figure 7).

The absence of GPCR-mediated cytosolic and mitochondrial Ca^{2+} dynamics in the yeast model system limits the role for EF hand domains. Until now, Miro1 was identified to transport mitochondria (motility) for local energy distribution through GTPase activity in Metazoans. Our data reveal the functional role of the conserved Ca^{2+} binding motifs rather GTPase domains for the previously undescribed MiST phenomenon. MiST is induced by mitochondrial localized Miro1 upon Ca^{2+} binding, and this mechanism is rapid and independent of $[Ca^{2+}]_m$ uptake. The cytosolic Ca^{2+}-sensing domain containing Miro1 is the determinant of MiST, which is required for alternate cell fate mechanism.

EXPERIMENTAL PROCEDURES

Simultaneous Measurement of Mitochondrial Shape and $[Ca^{2+}]_c$

HeLa WT cells were grown on 25-mm glass coverslips and transfected with COX8-mRFP. 48 hr post transfection, cells were treated for 30 min ± CsA (5 μM) and stained with PTP opening indicator calcein-AM. MiST and PTP opening were observed as detailed in Supplemental Experimental Procedures.

Simultaneous Assessment of MiST and Autophagy

Stable M1WT and M1EF1 mutant MEFs were transiently transfected with Cox8a-mRFP and LC3-GFP and LC3 translocation was assessed as detailed in Supplemental Experimental Procedures. To monitor the transfer of lipid from mitochondria to autophagosome during starvation-induced autophagy, M1WT and M1EF1 mutant MEFs were co-transfected with Mito-BFP and mCherry-LC3 and co-localization observed as detailed in Supplemental Experimental Procedures.

Size Exclusion Chromatographic Analysis of Miro1 Complex

Gel filtration of Miro1 complex was performed at 4°C by FPLC (ÄKTA Pure FPLC; GE Healthcare), using Superdex 200 10/300 column equilibrated with PBS. The cleared cell lysates prepared from MEFs stably expressing M1WT and MiEF1 mutant were directly loaded onto a Superdex 200 FPLC column at a flow rate of 0.5 mL/min. The 0.5-mL fractions were collected, concentrated, and used to assay complexes by immunoblotting.

Generation of Hepatocyte-Specific Mice and Isolation of Primary Hepatocytes

Hepatocyte-specific Mcu KOs were generated by a Cre-LoxP approach using hepatocyte-specific Cre-recombinase transgenic mice (B6.Cg-Tg(Alb-cre) 21Mgn/J, The Jackson Laboratory, USA) and $MCU^{fl/fl}$ mice. All animal experiments were approved by Temple University's Institutional Animal Care and Use Committee (IACUC) and followed Association for Assessment and Accreditation of Laboratory Animal Care (AAALAC) guidelines. Primary adult mouse hepatocytes were isolated using a two-step collagenase perfusion technique with slight modifications as detailed in Supplemental Experimental Procedures.

Statistical Analysis

Data were expressed as the mean ± SE. Statistical significance was evaluated via Student's unpaired t test, one-way and two-way ANOVA. $p < 0.05$ was considered statistically significant. All experiments were conducted at least three times unless specified. Data were plotted either with Sigma Plot 11.0 software or GraphPad Prism version 6 software. Data obtained from neurons were analyzed using GraphPad Instat software (v.3.10).

Supplementary Material

Refer to Web version on PubMed Central for supplementary material.

Acknowledgments

We thank Craig B. Thompson, Richard Youle, Gia Voeltz, Tom Rapoport, and Gary Yellen for sharing $Bax^{-/-}$ $Bak^{-/-}$ MEFs, mito-Keima, mito-BFP, sec61-β, and Peredox plasmid constructs, respectively. We thank John Elrod for sharing the CypD KO MEFs. The authors also thank Shannon Modla for EM sample processing and image acquisition. This research was funded by the NIH (R01GM109882, R01HL086699, R01HL119306, and 1S10RR027327 to M.M. and R01 NS095471 to G.G.). N.N. and D.T. are supported by the AHA fellowships (17PRE33660720, 17POST33660251). S.S. is supported by a NIH K99/R00 grant (1K99HL138268-01). Z.D. is supported by China Scholarship Council (No. 201403170252). F.J. is supported by FONDECYT postdoctoral fellowship #3140458. Access to the electron microscope was supported by NIH-NIGMS (P20 GM103446) and NSF (IIA-1301765).

References

Allen MD, Qamar S, Vadivelu MK, Sandford RN, Bycroft M. A high-resolution structure of the EF-hand domain of human polycystin-2. Protein Sci. 2014; 23:1301–1308. [PubMed: 24990821]

Baines CP, Kaiser RA, Purcell NH, Blair NS, Osinska H, Hambleton MA, Brunskill EW, Sayen MR, Gottlieb RA, Dorn GW, et al. Loss of cyclophilin D reveals a critical role for mitochondrial permeability transition in cell death. Nature. 2005; 434:658–662. [PubMed: 15800627]

Baughman JM, Perocchi F, Girgis HS, Plovanich M, Belcher-Timme CA, Sancak Y, Bao XR, Strittmatter L, Goldberger O, Bogorad RL, et al. Integrative genomics identifies MCU as an essential component of the mitochondrial calcium uniporter. Nature. 2011; 476:341–345. [PubMed: 21685886]

Bereiter-Hahn J, Vöth M. Dynamics of mitochondria in living cells: Shape changes, dislocations, fusion, and fission of mitochondria. Microsc Res Tech. 1994; 27:198–219. [PubMed: 8204911]

Berridge MJ, Bootman MD, Roderick HL. Calcium signalling: Dynamics, homeostasis and remodelling. Nat Rev Mol Cell Biol. 2003; 4:517–529. [PubMed: 12838335]

Birsa N, Norkett R, Higgs N, Lopez-Domenech G, Kittler JT. Mitochondrial trafficking in neurons and the role of the Miro family of GTPase proteins. Biochem Soc Trans. 2013; 41:1525–1531. [PubMed: 24256248]

Boldogh IR, Pon LA. Interactions of mitochondria with the actin cytoskeleton. Biochim Biophys Acta. 2006; 1763:450–462. [PubMed: 16624426]

Brustovetsky T, Li V, Brustovetsky N. Stimulation of glutamate receptors in cultured hippocampal neurons causes Ca2+-dependent mitochondrial contraction. Cell Calcium. 2009; 46:18–29. [PubMed: 19409612]

Cereghetti GM, Stangherlin A, Martins de Brito O, Chang CR, Black-stone C, Bernardi P, Scorrano L. Dephosphorylation by calcineurin regulates translocation of Drp1 to mitochondria. Proc Natl Acad Sci USA. 2008; 105:15803–15808. [PubMed: 18838687]

Clapham DE. Calcium signaling. Cell. 2007; 131:1047–1058. [PubMed: 18083096]

Claude A, Fullam EF. An electron microscope study of isolated mitochondria: Method and preliminary results. J Exp Med. 1945; 81:51–62. [PubMed: 19871443]

Cribbs JT, Strack S. Reversible phosphorylation of Drp1 by cyclic AMP-dependent protein kinase and calcineurin regulates mitochondrial fission and cell death. EMBO Rep. 2007; 8:939–944. [PubMed: 17721437]

De Stefani D, Raffaello A, Teardo E, Szabò I, Rizzuto R. A forty-kilodalton protein of the inner membrane is the mitochondrial calcium uniporter. Nature. 2011; 476:336–340. [PubMed: 21685888]

Denton RM. Regulation of mitochondrial dehydrogenases by calcium ions. Biochim Biophys Acta. 2009; 1787:1309–1316. [PubMed: 19413950]

Detmer SA, Chan DC. Functions and dysfunctions of mitochondrial dynamics. Nat Rev Mol Cell Biol. 2007; 8:870–879. [PubMed: 17928812]

Fransson A, Ruusala A, Aspenström P. Atypical Rho GTPases have roles in mitochondrial homeostasis and apoptosis. J Biol Chem. 2003; 278:6495–6502. [PubMed: 12482879]

Fransson S, Ruusala A, Aspenström P. The atypical Rho GTPases Miro-1 and Miro-2 have essential roles in mitochondrial trafficking. Biochem Biophys Res Commun. 2006; 344:500–510. [PubMed: 16630562]

Frederick RL, McCaffery JM, Cunningham KW, Okamoto K, Shaw JM. Yeast Miro GTPase, Gem1p, regulates mitochondrial morphology via a novel pathway. J Cell Biol. 2004; 167:87–98. [PubMed: 15479738]

Hailey DW, Rambold AS, Satpute-Krishnan P, Mitra K, Sougrat R, Kim PK, Lippincott-Schwartz J. Mitochondria supply membranes for autophagosome biogenesis during starvation. Cell. 2010; 141:656–667. [PubMed: 20478256]

Halestrap AP, Griffiths EJ, Connern CP. Mitochondrial calcium handling and oxidative stress. Biochem Soc Trans. 1993; 21:353–358. [PubMed: 8359495]

Høyer-Hansen M, Bastholm L, Szyniarowski P, Campanella M, Szabadkai G, Farkas T, Bianchi K, Fehrenbacher N, Elling F, Rizzuto R, et al. Control of macroautophagy by calcium, calmodulin-dependent kinase kinase-β, and Bcl-2. Mol Cell. 2007; 25:193–205. [PubMed: 17244528]

Kroemer G, Galluzzi L, Brenner C. Mitochondrial membrane permeabilization in cell death. Physiol Rev. 2007; 87:99–163. [PubMed: 17237344]

Lee JE, Westrate LM, Wu H, Page C, Voeltz GK. Multiple dynamin family members collaborate to drive mitochondrial division. Nature. 2016; 540:139–143. [PubMed: 27798601]

Losón OC, Song Z, Chen H, Chan DC. Fis1, Mff, MiD49, and MiD51 mediate Drp1 recruitment in mitochondrial fission. Mol Biol Cell. 2013; 24:659–667. [PubMed: 23283981]

Macaskill AF, Rinholm JE, Twelvetrees AE, Arancibia-Carcamo IL, Muir J, Fransson A, Aspenstrom P, Attwell D, Kittler JT. Miro1 is a calcium sensor for glutamate receptor-dependent localization of mitochondria at synapses. Neuron. 2009; 61:541–555. [PubMed: 19249275]

Mallilankaraman K, Cárdenas C, Doonan PJ, Chandramoorthy HC, Irrinki KM, Golenár T, Csordás G, Madireddi P, Yang J, Müller M, et al. MCUR1 is an essential component of mitochondrial Ca2+ uptake that regulates cellular metabolism. Nat Cell Biol. 2012; 14:1336–1343. [PubMed: 23178883]

Mishra P, Chan DC. Mitochondrial dynamics and inheritance during cell division, development and disease. Nat Rev Mol Cell Biol. 2014; 15:634–646. [PubMed: 25237825]

Murley A, Lackner LL, Osman C, West M, Voeltz GK, Walter P, Nunnari J. ER-associated mitochondrial division links the distribution of mitochondria and mitochondrial DNA in yeast. eLife. 2013; 2:e00422. [PubMed: 23682313]

Nguyen TT, Oh SS, Weaver D, Lewandowska A, Maxfield D, Schuler MH, Smith NK, Macfarlane J, Saunders G, Palmer CA, et al. Loss of Miro1-directed mitochondrial movement results in a novel murine model for neuron disease. Proc Natl Acad Sci USA. 2014; 111:E3631–E3640. [PubMed: 25136135]

Nicholls DG. Mitochondria and calcium signaling. Cell Calcium. 2005; 38:311–317. [PubMed: 16087232]

Narendra D, Tanaka A, Suen DF, Youle RJ. Parkin is recruited selectively to impaired mitochondria and promotes their autophagy. J Cell Biology. 2008; 183:795–803.

Orrenius S, Zhivotovsky B, Nicotera P. Regulation of cell death: The calcium-apoptosis link. Nat Rev Mol Cell Biol. 2003; 4:552–565. [PubMed: 12838338]

Pagliarini DJ, Calvo SE, Chang B, Sheth SA, Vafai SB, Ong SE, Walford GA, Sugiana C, Boneh A, Chen WK, et al. A mitochondrial protein compendium elucidates complex I disease biology. Cell. 2008; 134:112–123. [PubMed: 18614015]

Palmer CS, Osellame LD, Laine D, Koutsopoulos OS, Frazier AE, Ryan MT. MiD49 and MiD51, new components of the mitochondrial fission machinery. EMBO Rep. 2011; 12:565–573. [PubMed: 21508961]

Pan X, Liu J, Nguyen T, Liu C, Sun J, Teng Y, Fergusson MM, Rovira II, Allen M, Springer DA, et al. The physiological role of mitochondrial calcium revealed by mice lacking the mitochondrial calcium uniporter. Nat Cell Biol. 2013; 15:1464–1472. [PubMed: 24212091]

Reis K, Fransson A, Aspenström P. The Miro GTPases: At the heart of the mitochondrial transport machinery. FEBS Lett. 2009; 583:1391–1398. [PubMed: 19376118]

Rintoul GL, Filiano AJ, Brocard JB, Kress GJ, Reynolds IJ. Glutamate decreases mitochondrial size and movement in primary forebrain neurons. J Neurosci. 2003; 23:7881–7888. [PubMed: 12944518]

Rowland AA, Voeltz GK. Endoplasmic reticulum-mitochondria contacts: Function of the junction. Nat Rev Mol Cell Biol. 2012; 13:607–625. [PubMed: 22992592]

Saotome M, Safiulina D, Szabadkai G, Das S, Fransson A, Aspenstrom P, Rizzuto R, Hajnóczky G. Bidirectional Ca2+-dependent control of mitochondrial dynamics by the Miro GTPase. Proc Natl Acad Sci USA. 2008; 105:20728–20733. [PubMed: 19098100]

Schwarz, TL. Mitochondrial trafficking in neurons; Cold Spring Harb Perspect Biol. 2013. p. 10https://doi.org/10.1101/cshperspect.a011304

Shanmughapriya S, Rajan S, Hoffman NE, Higgins AM, Tomar D, Nemani N, Hines KJ, Smith DJ, Eguchi A, Vallem S, et al. SPG7 is an essential and conserved component of the mitochondrial permeability transition pore. Mol Cell. 2015; 60:47–62. [PubMed: 26387735]

Smith AC, Blackshaw JA, Robinson AJ. MitoMiner: A data warehouse for mitochondrial proteomics data. Nucleic Acids Res. 2012; 40:D1160–D1167. [PubMed: 22121219]

Soboloff J, Rothberg BS, Madesh M, Gill DL. STIM proteins: Dynamic calcium signal transducers. Nat Rev Mol Cell Biol. 2012; 13:549–565. [PubMed: 22914293]

Tan AR, Cai AY, Deheshi S, Rintoul GL. Elevated intracellular calcium causes distinct mitochondrial remodelling and calcineurin-dependent fission in astrocytes. Cell Calcium. 2011; 49:108–114. [PubMed: 21216007]

Tanaka Y, Kanai Y, Okada Y, Nonaka S, Takeda S, Harada A, Hirokawa N. Targeted disruption of mouse conventional kinesin heavy chain, kif5B, results in abnormal perinuclear clustering of mitochondria. Cell. 1998; 93:1147–1158. [PubMed: 9657148]

Wang X, Schwarz TL. The mechanism of Ca2+ dependent regulation of kinesin-mediated mitochondrial motility. Cell. 2009; 136:163–174. [PubMed: 19135897]

Yaffe MP. The machinery of mitochondrial inheritance and behavior. Science. 1999; 283:1493–1497. [PubMed: 10066164]

Youle RJ, van der Bliek AM. Mitochondrial fission, fusion, and stress. Science. 2012; 337:1062–1065. [PubMed: 22936770]

Highlights

- Mitochondria shape transition (MiST) is driven by metazoan cytosolic Ca^{2+} signal
- MiST is distinct from mitochondrial swelling and fission processes
- Miro1 is a cytosolic Ca^{2+} sensor that determines MiST through EF-hand 1 domain
- Miro-dependent MiST is a prerequisite for mitochondrial quality control

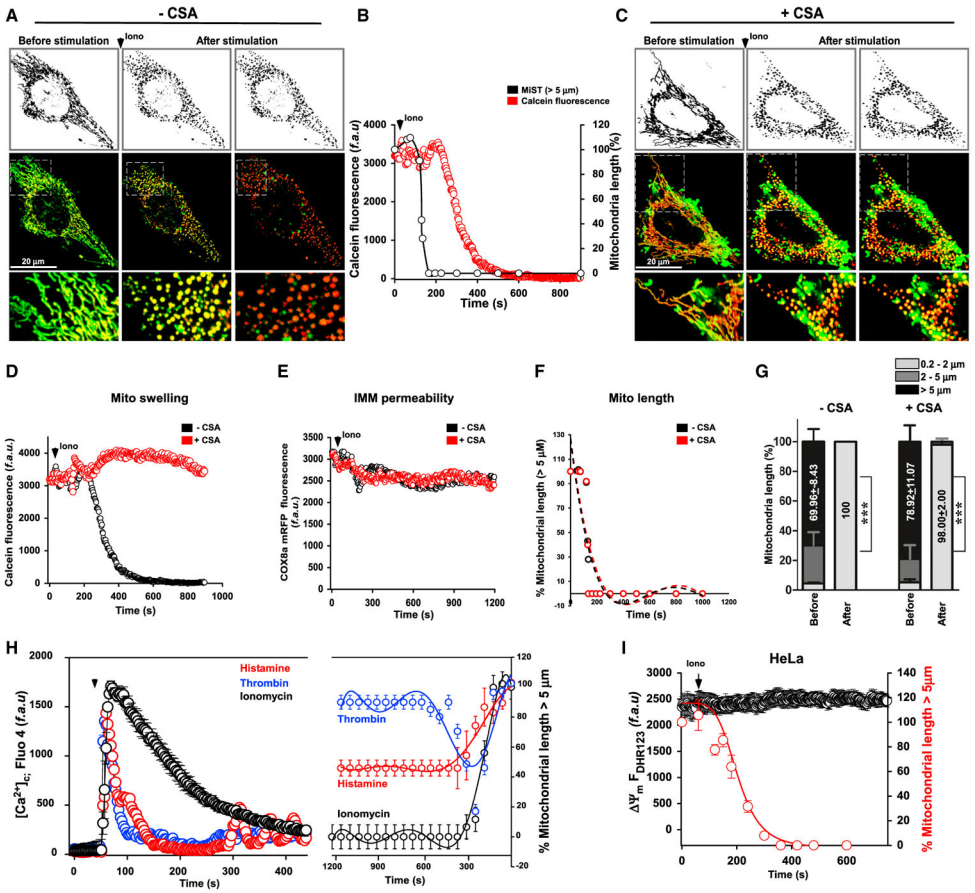

Figure 1. $[Ca^{2+}]_c$ Elicits MiST That Is Independent of Mitochondrial Swelling

(A) Representative images of live HeLa cells transiently transfected with Cox8a-mRFP and loaded with calcein-AM (1 µM) in the presence of $CoCl_2$ (1 mM). Cells were challenged with ionomycin (iono; 2.5 µM) and imaged for a total of 20 min.

(B) Representative traces of calcein fluorescence (red) and mitochondrial length change over time (black). n = 6.

(C) As in (A), representative images of HeLa cells expressing Cox8a-mRFP, loaded with calcein-AM + $CoCl_2$ and in the presence of CsA (5 µM).

(D) Representative traces of calcein fluorescence. n = 6.

(E) Representative traces of cox8a-mRFP fluorescence. n = 6.

(F) Mean traces of mitochondria >5 µm in length calculated from Figures 1A and 1C. Mean ± SEM; n = 6.

(G) Quantification of MiST in – CsA and + CsA conditions calculated from Figures 1A and 1C. Mean ± SEM; n = 6. ***p < 0.001 (p value calculated for 0.2- to 2-µm-length mitochondria).

(H) Mean traces of $[Ca^{2+}]_c$ (Fluo-4) responses in WT HeLa and MEFs stimulated with GPCR agonists (histamine [100 µM], thrombin [5 mU/mL]) and iono (2.5 µM). Right: depicts MiST. Mean ± SEM; n = 3.

(I) Mean traces of $\Delta\Psi_m$ (black) and MiST (red) following iono (2.5 µM) stimulation in HeLa cells. Mean ± SEM; n = 4. subjected to ionomycin stimulation, both hepatocytes

exhibited a rapid MiST (Figures 2E and 2F). Remarkably, $[Ca^{2+}]_m$-induced dissipation of DHR123 was only observed in $MCU^{fl/fl}$ but not

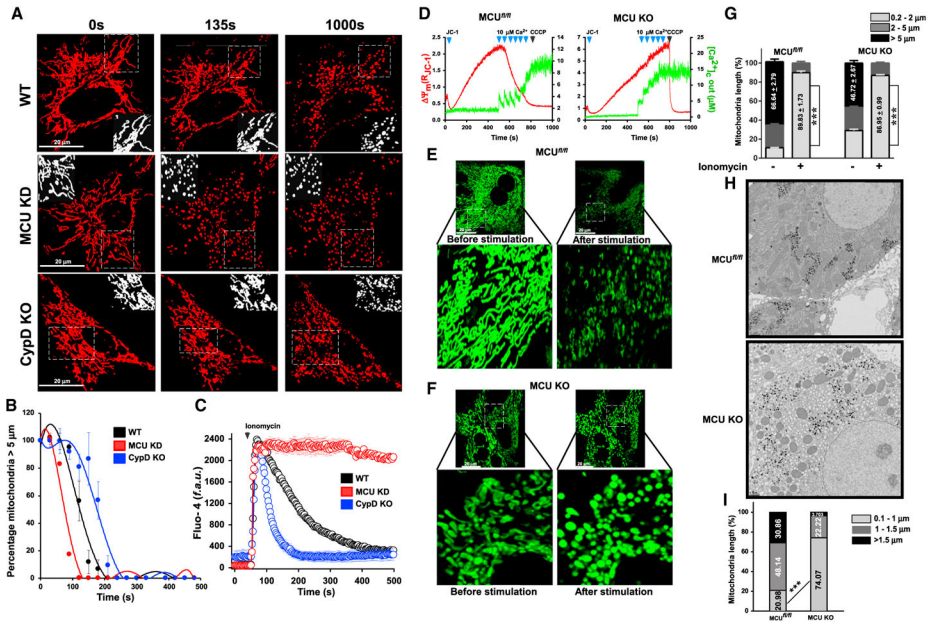

Figure 2. MiST Is Independent of MCU-Mediated $[Ca^{2+}]_m$ Loading

(A) Real-time visualization of MiST in WT, MCU KD HeLa, and CypD KO MEFs expressing cox8a-mRFP and stimulated with iono. (B) Mean traces of MiST over time from Figure 2A. Mean ± SEM; n = 6.

(C) Mean traces of $[Ca^{2+}]_c$ (Fluo-4) signal after stimulation with iono. Mean ± SEM; n = 6.

(D) Representative traces of $[Ca^{2+}]_{out}$ clearance (green) and $\Delta\Psi_m$ (red) in hepatocytes isolated from $MCU^{fl/fl}$ and $MCU^{-/-}$ mice.

(E and F) Representative confocal images of live $MCU^{fl/fl}$ and $MCU^{-/-}$ primary hepatocytes loaded with DHR123 and challenged with iono (2.5 µM) n = 7.

(G) Bar graph represents MiST in $MCU^{fl/fl}$ and $MCU^{-/-}$ hepatocytes. Mean ± SEM; (n = 6). ***p < 0.001.

(H) Representative EM images depicting the change in mitochondrial morphology in $MCU^{fl/fl}$ and $MCU^{-/-}$ liver (n = 3 mice).

(I) Analysis of MiST from EM images. Mean ± SEM; n = 3. ***p < 0.001 (p value calculated for 0.1- to 1-µm-length mitochondria).

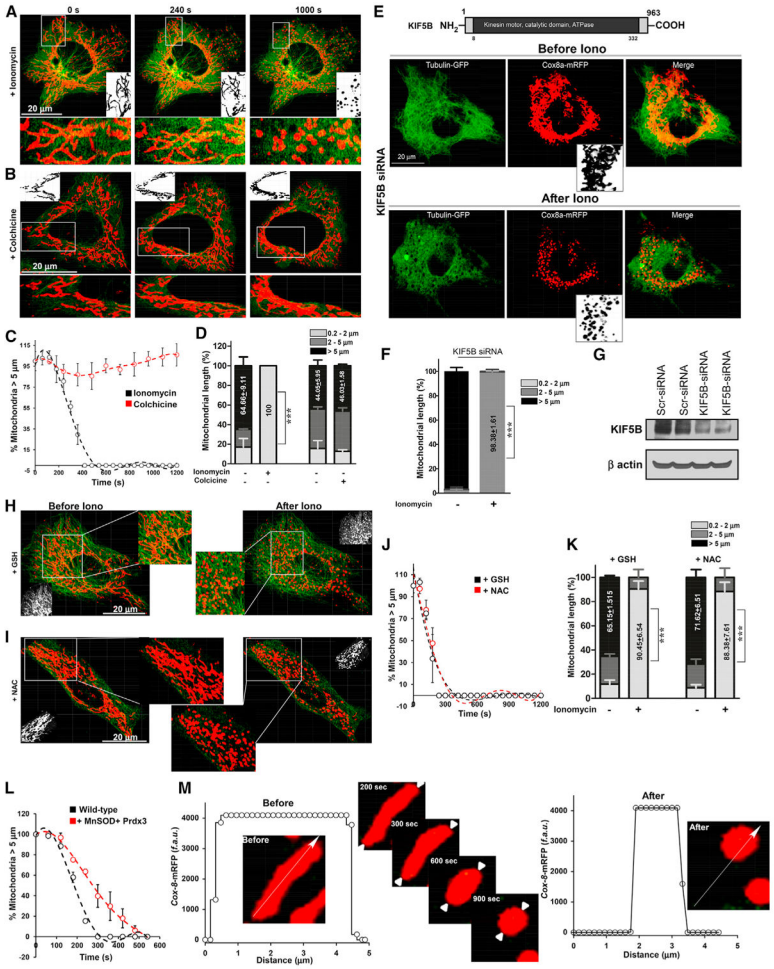

Figure 3. MiST Is Independent of Microtubule Changes and ROS

(A and B) Real-time visualization of MiST in HeLa cells expressing cox8a-mRFP and tubulin-GFP challenged with iono (A) or colchicine (B) (1 μM).

(C) Mean traces of MiST from HeLa cells treated with iono and colchicine from Figures 3A and 3B. Mean ± SEM; n = 8.

(D) Quantification of MiST from Figures 3A and 3B. Mean ± SEM; n = 3. ***p < 0.001.

(E) Scheme shows the KIF5B domains. Real-time visualization of MiST in KIF5B siRNA-treated MEFs.

(F) Quantification of MiST. Mean ± SEM; n = 3–6.

(G) Immunoblot shows the RNAi-mediated knockdown of KIF5B in MEFs.

(H and I) Representative images of HeLa cells expressing cox8a-mRFP and tubulin-GFP pretreated with GSH-ester (5 mM) (H) and N-Acetyl cysteine (10 mM) (I).

(J) Mean traces of MiST over time were derived from (H) and (I). Mean ± SEM; n = 3.

(K) Quantification of MiST from Figures 3H and 3I. Mean ± SEM. ***p < 0.001.

(L) Mean traces of MiST over time from control and AdMnSOD and peroxiredoxin 3 (PRDX3)-expressing HeLa cells. Mean ± SEM; n = 3.

>M) Line scanning data representing the mitochondrion undergoing MiST over time.

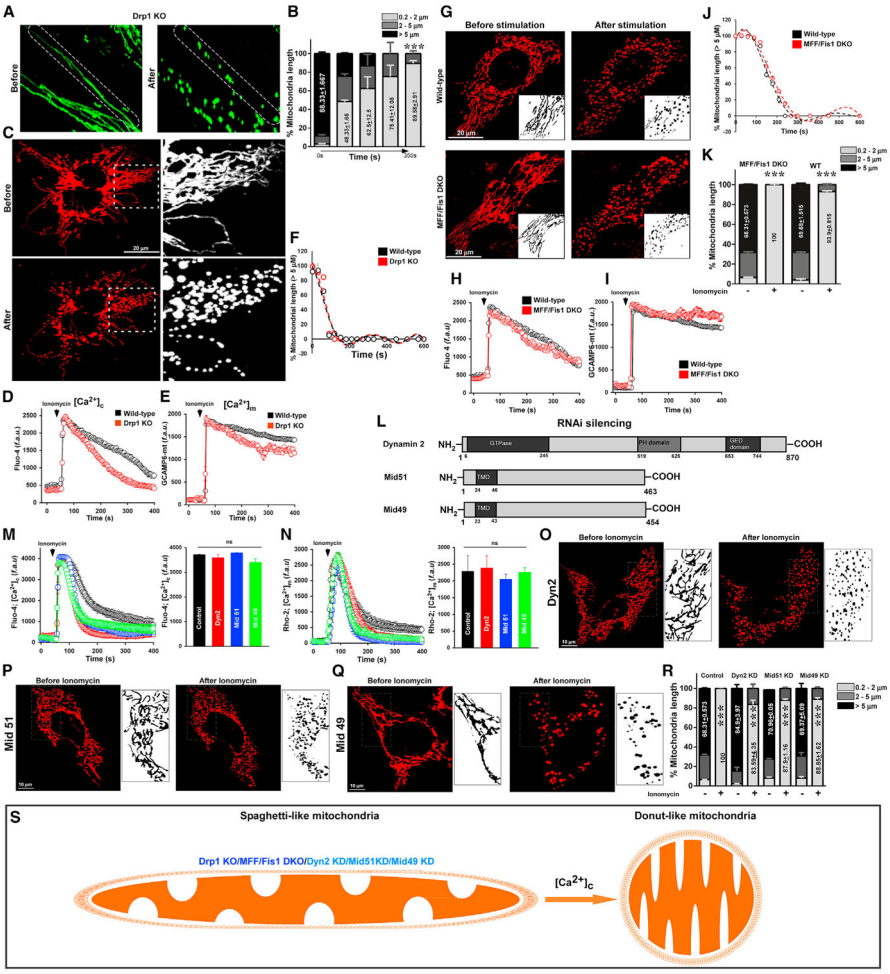

Figure 4. Ca^{2+}-Induced MiST Is Independent of Mitochondrial Fission Machinery

(A) Representative confocal images depicting MiST in Drp1 KO MEFs transfected with GCaMP6-mt and challenged with iono. n = 10.

(B) Bar graph represents MiST over time in Drp1 KO MEFs. Mean ± SEM; n = 6. ***p < 0.001.

(C) Representative confocal images depicting MiST in Drp1 KO MEFs expressing cox8a-mRFP. n = 10.

(D and E) Mean traces of $[Ca^{2+}]_c$ (Fluo 4) (D) and $[Ca^{2+}]_m$ (GCaMP6-mt)

(E) uptake in WT and Drp1 KO MEFs upon stimulation with iono. Mean ± SEM; n = 10.

(F) Mean traces of MiST over time. Mean ± SEM; n = 10.

(G) Representative images showing MiST in WT and MFF/Fis1 DKO MEFs expressing cox8a-mRFP and challenged with iono (2.5 μM).

(H and I) Mean traces of $[Ca^{2+}]_c$ (Fluo 4) (H) and $[Ca^{2+}]_m$ (GCaMP6-mt) (I) uptake in WT and MFF/Fis1 DKO MEFs upon stimulation with iono. Mean ± SEM; n = 6

(J) Mean traces of change in MiST over time Mean ± SEM; n = 8.

(K) Quantification of MiST. Mean ± SEM; n = 3, ***p < 0.001.

(L) Schematic representing full-length Dynamin 2, Mid51, and Mid49 domains.

(M and N) Mean traces of $[Ca^{2+}]_c$ (Fluo-4) (M) and $[Ca^{2+}]_m$ (rhod-2) (N) in Scr siRNA, Dyn2, Mid51, and Mid49 siRNA-treated MEFs stimulated with iono (2.5 μM). The bar graph (right) depicts the amplitude of Fluo-4 and rhod-2 fluorescence. Mean ± SEM; n = 3.
(O–Q) Real-time visualization of MiST in Dyn2 siRNA (O), Mid51 siRNA (P), and Mid49 siRNA (Q) MEFs.
(R) Quantification of MiST. Mean ± SEM; ***$p < 0.001$ n = 4–6.
(S) Cartoon depicting MiST in Drp1 KO, MFF/Fis1 DKO, and Dyn2, Mid51, and Mid49 KD MEFs.

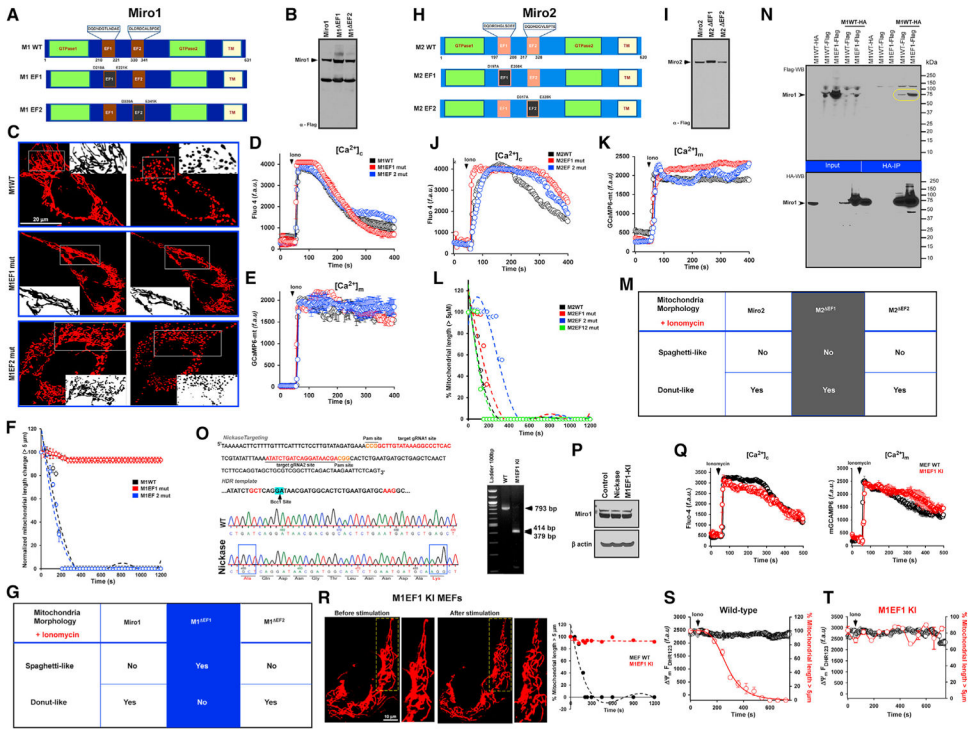

Figure 5. Miro1EF1 Is a Determinant of $[Ca^{2+}]_C$-Induced MiST

(A) Schematic representing full-length Miro1 and EF-hand mutation regions.

(B) Western blot analysis of cell lysates from MEFs stably expressing Flag-tagged -M1WT, -M1EF1, and -M1EF2 mutants probed with Flag antibody.

(C) Representative images of MiST in M1WT, M1EF1, and M1EF2 mutants MEFs transfected with cox8a-mRFP when challenged with iono.

(D and E) Mean traces of $[Ca^{2+}]_c$ (Fluo-4)

(D) and $[Ca^{2+}]_m$ (GCaMP6-mt)

(E) uptake in WT, M1EF1 mutant, and M1EF2 mutant MEFs stimulated with iono. Mean ± SEM; n = 6–12.

(F) Mean traces of MiST over time from WT, M1EF1, and M1EF2 mutants. Mean ± SEM; n = 3.

(G) Table summarizing the MiST events in WT and EF mutants of Miro1.

(H) Schematic representing full-length Miro2 and EF-hand mutation regions.

(I) Western blot analysis of cell lysates from MEFs expressing Flag-tagged -M2WT, -M2EF1, and -M2EF2 mutants probed with Flag antibody (n = 3).

(J and K) Mean traces of $[Ca^{2+}]_c$ (Fluo-4) (D) and $[Ca^{2+}]_m$ (GCaMP6-mt) (E) uptake in WT, M2EF1, and M2EF2 mutant MEFs stimulated with iono. Mean ± SEM; n = 6–12.

(L) Mean traces of MiST over time from WT, M2EF1 mutant, M2EF2 mutant and M2EF1/2 double mutant. Mean ± SEM; n = 3.

(M) Table summarizing the MiST events in WT and EF mutants of Miro2.

(N) Cell lysates or immunoprecipitated materials from HEK293T cells expressing FLAG-tagged M1WT, M1EF1 mutant, HA-tagged M1WT plasmids either individually or in combination as indicated and immunoblotted for FLAG or HA (n = 3).

(O) Schematic of M1EF1 knockin strategy. Gain of Bcc1 is a resultant of the knockin mutation at positions 1and 12. Bottom: represents sequencing of knockin positive clone. Right: depicts RFLP analysis.

(P) Immunoblot for Miro1 in control, nickase stable, and Miro1EF1-knockin MEFs.

(Q) Mean traces of $[Ca^{2+}]_c$ (Fluo-4) and $[Ca^{2+}]_m$ (GCaMP6-mt) uptake in WT, M1EF1 Knockin MEFs stimulated with iono. Mean ± SEM; n = 6–12.

(R) Representative images showing absence of MiST in M1EF1 knockin clone after challenge with iono. Right: represents quantification of MiST in WT and M1EF1 KI MEFs. n = 12.

(S and T) Mean traces of mitochondrial morphology and $\Delta\Psi_m$ changes from WT (S) and M1EF1 knockin (T) MEFs treated with iono. Mean ± SEM; n = 6.

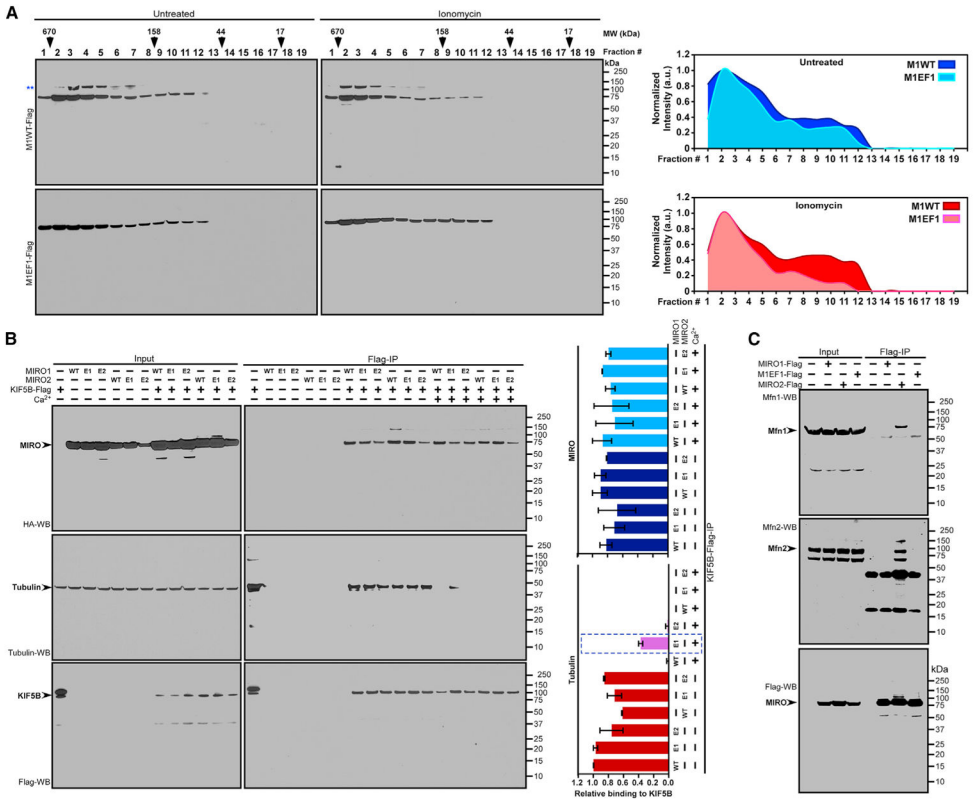

Figure 6. Miro1 EF1 Domain Determines The Binding of Miro1/KIF5B/Tubulin Complex in a Ca^{2+}-Dependent Fashion

(A) Cell lysates from control and ionomycin (2.5 μM for 30 min)-treated MEFs stably expressing Flag-tagged M1WT and M1EF1 mutants were subjected to FPLC analysis and probed with Flag antibody. Right: depicts the M1WT and M1EF1 complex elution profiles. **Super-shift of M1WT under both conditions (n = 2).

(B) Cell lysates input (left) and immunoprecipitated product (right) from MEF cells expressing Flag-tagged KIF5B and HA-tagged Miro1-WT, Miro1EF1, Miro1EF2, Miro2WT, Miro2EF1, and Miro2EF2 mutants in the presence or absence of Ca^{2+} (1 mM) were probed with HA, Flag, and tubulin antibodies. Bar chart represents densitometric analysis of Miro1, Miro2, and tubulin binding to KIF5B. Mean ± SEM; n = 3.

(C) Cell lysates input (left) and immunoprecipitated product (right) from MEFs expressing Miro1-Flag, Miro2-Flag, and Miro1EF1-Flag were immunoblotted with Flag, Mfn1, and Mfn2 antibodies (n = 3).

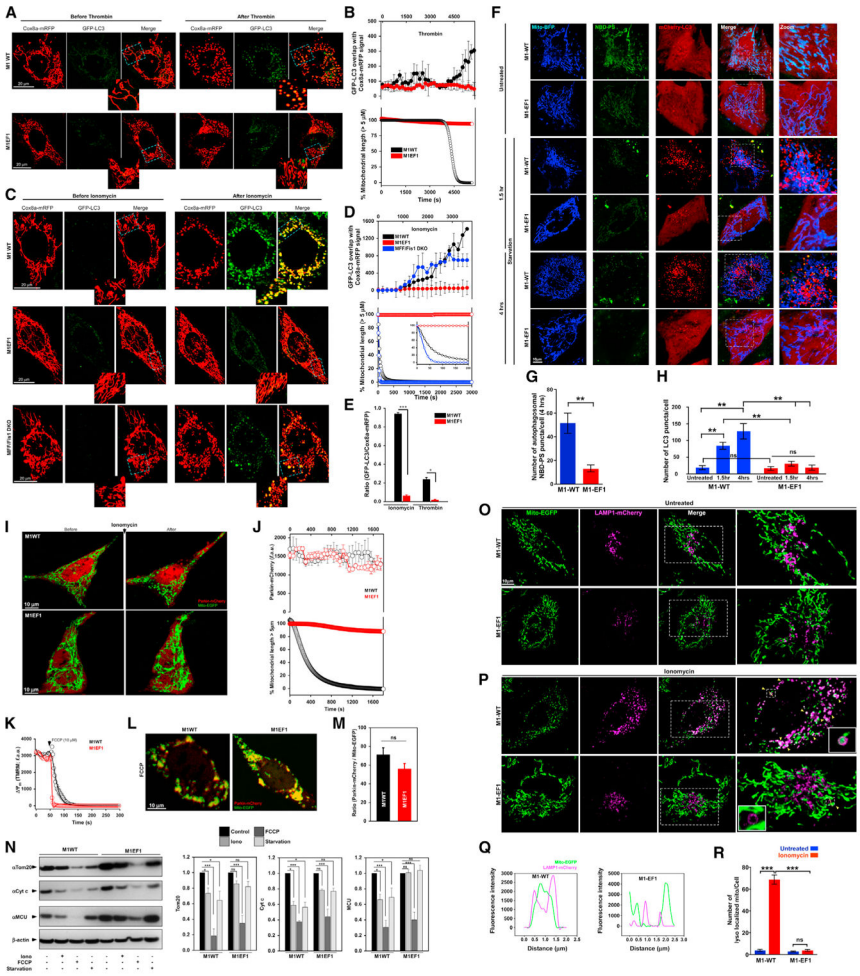

Figure 7. Cells Harboring Miro1 EF1 Mutant Do Not Form Autophagosomes in Response to GPCR and Stress-Mediated Ca^{2+} Transients

(A) Representative confocal images of M1WT and M1EF1 mutant MEFs co-transfected with cox8a-mRFP and GFP-LC3 challenged with thrombin (15 mU/mL).

(B) Mean traces of GFP-LC3 overlap with Cox8a-mRFP fluorescence (top) and MiST over time (bottom) from M1WT and M1EF1 mutant MEFs (top). Mean ± SEM; n = 6.

(C) Representative confocal images of M1WT and M1EF1 mutant MEFs co-transfected with cox8a-mRFP and GFP-LC3 challenged with ionomycin (1 μM). MFF/Fis1 DKO MEFs were used as control.

(D) Mean traces of GFP-LC3 overlap with Cox8a-mRFP fluorescence (top) and MiST over time (bottom) from M1WT, M1EF1 mutant, and MFF/Fis1 DKO MEFs. Mean ± SEM; n = 6.

(E) The ratio of mitochondrial cox8a-mRFP overlay with GFP-LC3. Mean ± SEM; n = 3. *p < 0.05; ***p < 0.001

(F) Representative images showing NBD-PS translocation to mitochondria and autophagosomes in MEFs expressing M1WT and M1EF1 mutant transfected with Mito-BFP and mCherry-LC3 followed by live-cell NBD-PS staining. n = 6 (30–40 cells).

(G) Quantification of NBD-PS translocation to autophagosome in Figure 7F. Mean ± SEM; n = 6, **p < 0.01.
(H) Quantification of autophagosome (LC3 puncta) number per cell in Figure 7F. Mean ± SEM; n = 6, ns (non-significant), **p < 0.01.
(I) Visualization of MiST and Parkin translocation in MEFs expressing M1WT and M1EF1 mutant were transfected with Parkin-mCherry and mito-EGFP following iono stimulation. n = 4.
(J) Mean traces of Parkin-mCherry overlap with Mito-EGFP fluorescence (top) and MiST (bottom) from M1WT and M1EF1 mutant MEFs. Mean ± SEM; n = 4
(K) Mean traces of mitochondrial depolarization induced by FCCP (10 μM). Mean ± SEM; n = 3.
(L) Representative images of MEFs expressing M1WT and M1EF1 mutant transfected with Parkin-mCherry and mito-EGFP and treated with 10 μM FCCP for 4 hr to visualize Parkin translocation. n = 3 (20–30 cells).
(M) Quantification of Parkin-mCherry/mito-EGFP puncta. n = 3 (20–30 cells). Mean ± SEM; ns, not significant.
(N) Western blot analysis for Tom20, cytochrome *c*, and MCU in M1WT and M1EF1 mutant MEFs treated with FCCP (10 μM), iono (5 μM), or starvation for 16 hr (left). Densitometric analysis (right). Mean ± SEM; n = 2. *p < 0.05, ***p < 0.001
(O and P) Representative images of M1WT and M1EF1 mutant MEFs co-transfected with Mito-EGFP and Lamp1-mCherry (O) before and (P) after treatment with 5 μM iono for 4 hr and lyso/mito phagosome formation was monitored.
(Q) Line-scan data from lysosomal localized mitochondria after treatment with iono.
(R) Quantification of lysosomal localized mitochondria. Mean ± SEM; n = 4. ***p < 0.001